ELSEVIER

Contents lists available at ScienceDirect

Chemical Engineering Journal

journal homepage: www.elsevier.com/locate/cej





Manganese alchemy: Atomic-scale doping to miniaturize cobalt oxide in nanofiber architecture for ultra-fast lithium-ion batteries

Hyunmin Na a,b,1 , Ho-Jin Lee a,b,1 , Dae-Kwon Boo a,b , Ilgyu Kim a , Jeong-Ho Park a,c , Jae-Woo Seo d , Seon-Jin Choi d , Jiyoung Lee e , Tae Gwang Yun f , Byungil Hwang g , Jun Young Cheong h,* , Ji-Won Jung a,b,**

- ^a Department of Materials Science and Engineering, Konkuk University, 120, Neungdong-ro, Gwangjin-gu, Seoul 05029, Republic of Korea
- b Department of Materials Science and Engineering, Advanced Materials Program, Konkuk University, 120, Neungdong-ro, Gwangjin-gu, Seoul 05029, Republic of Korea
- ^c School of Materials Science and Engineering, University of Ulsan, Techno Saneop-ro 55 Beon-gil, Nam-gu, Ulsan 44776, Republic of Korea
- d Division of Materials Science and Engineering, Hanyang University, Advanced Materials & Chemical Engineering Building, 222 Wangsimni-ro, Seongdong-gu, Seoul 04763. Republic of Korea
- e Department of Chemical Engineering, Ajou University, Suwon 16499, Republic of Korea
- f Department of Molecular Science and Technology, Ajou University, Suwon 16499, Republic of Korea
- g School of Integrative Engineering, Chung-Ang University, Building 310, 84 Heukseok-ro, Dongjak-gu, Seoul 06974, Republic of Korea
- ^h James Watt School of Engineering, University of Glasgow, Glasgow G12 8QQ, UK

ARTICLE INFO

Keywords: Lithium-ion batteries Anodes Cobalt oxides Doping Grain size

ABSTRACT

Lithium-ion batteries (LIBs) are essential for modern portable electronics and future mobility solutions, yet improving fast-charging capabilities and cycling stability remains a considerable challenge. This study investigates a new strategy to enhance LIB anode performance by incorporating manganese (Mn)-doped (0, 0.05, 0.1, and 0.2 at.%) cobalt oxide (Co_3O_4) nanofibers. Mn doping facilitates the downsizing of Co_3O_4 nanograins interconnected along the one-dimensional nanofibers by inducing lattice distortions and creating oxygen vacancies, which improve electronic conductivity and reactivity. The integration of Mn dopants into the Co_3O_4 host reduces grain size, shortens Li^+ diffusion pathways, and increases the Li-ion accessible area, thereby enhancing electron/ Li^+ transport and cycling stability. The LIB cell with the optimized Mn doping level (0.2 at.%) achieves minimized side reactions, a high specific capacity of 1237 mAh g^{-1} at 500 mA g^{-1} after 300 cycles, and an impressive capacity of 490 mAh g^{-1} even at an extremely high current density of 5 A g^{-1} . This study advances LIB anode design through tailored doping engineering to control grain size, achieving desired structural and electrochemical properties and providing valuable insights for sustainable energy technologies.

1. Introduction

Despite the rapidly growing market and considerable advancements in lithium-ion batteries (LIBs) [1–4], the increasing demand for superior LIBs requires continuous progress in fast-chargeable materials technology [5,6]. Such advancements are critical for enhancing user convenience by reducing charging time, particularly for applications in industries such as logistics and public transportation [7]. Among the essential physical properties, high—capacity anodes designed for fast charging and discharging require reduced thickness. This reduction

enables efficient Li⁺ ionic and electronic conduction through short, low-tortuosity pathways between the electrode surface and the current collector [8]. Current commercial graphite materials have a limited specific capacity of 372 mAh g⁻¹ requiring relatively thick electrodes that are prone to structural collapse under fast (dis)charging protocols at high C-rates [9–12]. These thick graphite electrodes are often inefficient because they increase battery volume and hinder ion flow during fast charging, ultimately compromising conductivity and stability between the electrode and the current collector. As a result, innovative and unconventional strategies are urgently needed to develop high-capacity,

^{*} Corresponding author.

^{**} Corresponding author at: Department of Materials Science and Engineering, Konkuk University, 120, Neungdong-ro, Gwangjin-gu, Seoul 05029, Republic of Korea.

 $[\]textit{E-mail addresses:} \ junyoung. cheong@glasgow.ac.uk \ (J.Y.\ Cheong), jwjung4@konkuk.ac.kr \ (J.-W.\ Jung).$

 $^{^{1}\,}$ These authors contributed equally to this work.

fast-chargeable anode materials for LIBs. For instance, Jing et al. engineered oxygen-deficient $T\text{-Nb}_2O_5$ nanosheets to enhance Li^+ diffusivity and electrical conductivity, thereby achieving excellent rate capability and long-term cycling stability [13]. Similarly, Liu et al. synthesized defect-rich $Ti_2Nb_{10}O_{29}$ microspheres via a dual-carbon strategy, which provided abundant ion diffusion channels and electronic pathways, resulting in outstanding fast-charging performance and structural stability [14]. Furthermore, Feng et al. employed a tailored nanoarchitecture of $Li_4Ti_5O_{12}$ to achieve a high reversible capacity with superior rate performance and cyclability, taking advantage of its intrinsic zero-strain characteristics [15]. Despite their rate capabilities, these materials are often constrained by relatively low specific capacities. To overcome this limitation, research has increasingly focused on transition metal oxides that can deliver much higher capacities through multi-electron conversion reactions.

Considerable attention has been focused on transition metal oxides such as MnO, Co₃O₄, Fe₃O₄, ZnO, MnO₂, NiO, and Fe₂O₃, recognized for their high capacities enabled by conversion reactions [16,17]. Among these, cobalt oxide (Co₃O₄) stands out owing to its excellent chemical stability and exceptionally high theoretical specific capacity (890 mAh g⁻¹), which arises from its ability to accommodate more than eight Li atoms per formula unit. However, achieving fast Li⁺ recharging and long-term durability with Co₃O₄ requires ensuring short transport paths for both electrons and Li⁺ ions. Nanostructuring is a key strategy for increasing contact area and maintaining structural stability under rapid charging and discharging conditions. For instance, Xiao Li et al. developed porous CoO/Co₃O₄ nanoribbons with mesoporous/macroporous structures and oxygen vacancies, achieving prolonged cycling life and high specific capacity [18]. Similarly, Yifan Zhang and colleagues created flower-like NiO/Co₃O₄ structures with numerous pores on the petals, demonstrating superior performance compared to the individual components [19]. However, these approaches have limitations such as complex and time-consuming fabrication processes, as well as limited stability and rate performance, which hinder the full realization of Co₃O₄ potential.

In this work, we aimed to develop fast-chargeable LIBs by leveraging manganese (Mn)-doping engineering in nanofibrous Co₃O₄ anode materials. The Mn-dopant concentration (c) was used to tailor the physicochemical properties of nanofibrous Mn-doped binary Co₃O₄ compounds (nf-(c)-MCO), enhancing rate and cycling performance by promoting the miniaturization of Co₃O₄ nanograins and improving ionic and electronic transport. Rigorous analyses were performed to elucidate how Mn-dopants influence the reduction in Co₃O₄ nanograin size and the correlations between material properties (oxidation state, oxygen vacancies, and band gap) and electrochemical battery performance. Smaller Co₃O₄ nanograins were achieved with increasing Mn-dopant content in the nf-(c)-MCO compounds, with nf-2-MCO (0.2 at.% Mn dopants) emerging as the optimized composition for superior rate capability and durability. The LIB cells with nf-2-MCO anodes demonstrated an impressive specific capacity of 1237 mAh g⁻¹ at 500 mA g⁻¹ after 300 cycles and excellent rate performance, maintaining a capacity of 490 mAh g⁻¹ even at a high current density of 5000 mA g⁻¹. These results highlight the potential of doping engineering to optimize the relationship between physicochemical properties and performance, offering valuable insights for advancements in energy technology.

2. Experimental

2.1. Materials

Cobalt acetate tetrahydrate ((CH $_3$ COO) $_2$ Co·4H $_2$ O) and manganese (II) acetate tetrahydrate ((CH $_3$ COO) $_2$ Mn·4H $_2$ O) were purchased from Sigma Aldrich, along with polyvinylpyrrolidone (PVP) and poly(acrylic acid) (PAA) ((C $_3$ H $_4$ O $_2$) $_n$). Carboxymethylcellulose sodium salt (CMC) was obtained from Nippon Paper Industries Co. The synthesis of manganese (Mn)-doped Co $_3$ O $_4$ nanofibers was performed to create an anode

material suitable for LIBs. The electrode was fabricated using a composite of Co_3O_4 , conductive carbon black (C.B), and a CMC-PAA binder. The electrode was enhanced with a proprietary vinylene carbonate (VC) additive to improve stability. The electrolyte solution was prepared by dissolving 1.3 M lithium hexafluorophosphate (LiPF₆) in a solvent mixture of ethylene carbonate (EC), ethyl methyl carbonate (EMC), and diethyl carbonate (DEC) in a volumetric ratio of 3:5:2. The VC additive was included at a concentration of 0.5 wt%, while fluoroethylene carbonate (FEC) and propylene sulfite (PS) additives were added at concentrations of 10 and 1 wt%, respectively. Electrodes were fabricated with various mass loadings, with 1.5 mg cm $^{-2}$ being the standard mass loading used in most experimental procedures.

2.2. Synthesis of nf-(c)-MCO anode materials

A mixture of 0.75 g (14.29 wt%) of cobalt acetate tetrahydrate, varying amounts of manganese (II) acetate tetrahydrate (0 g for *nf*–CO, 0.05 g for *nf*-1-MCO, 0.1 g for *nf*-2-MCO, and 0.2 g for *nf*-4-MCO), 0.5 g (9.52 wt%) of PVP, and 4 g (76.19 wt%) of dimethylformamide (DMF, 99.8 %) was stirred at room temperature for a period ranging from 4 to 12 h. The resulting solution was loaded into a syringe using a 25 G needle. Electrospinning was performed at an operating voltage of 16 kV, with a flow rate of 10 μL min⁻¹, and the distance between the syringe and collector was maintained at 15 cm. Nanofibers were collected on a collector coated with aluminum foil. The collected samples were heat-treated at 600 °C for 1 h in air, with a heating rate of 10 °C min⁻¹. The synthesis of nf-(c)-MCO was performed using a modified electrospinning method. The precursor solution was prepared by mixing cobalt acetate and manganese acetate in the desired proportions. The solution was then loaded into a syringe fitted with a specially designed needle for electrospinning. The electrospinning process was carefully controlled by adjusting key parameters such as applied voltage, flow rate, and spinning distance. The nanofibers were collected in their as-spun form on a collector coated with aluminum foil. Afterward, the specimens were annealed in ambient air at a predetermined temperature for a specified duration.

2.3. Materials characterizations

The synthesized nf-(c)-MCO nanofibers were comprehensively analyzed using a range of characterization techniques. X-ray diffraction (XRD) was used to investigate the crystal structure and phase composition while scanning electron microscopy (SEM) was used to examine the surface morphology and structural features. Raman spectroscopy provided insights into vibrational modes and molecular structure. To further analyze the internal structure and nanoscale morphology, transmission electron microscopy (TEM) and high-resolution TEM (HR-TEM) were used, along with scanning transmission electron microscopy (STEM) for atomic-level imaging. The surface area and pore distribution were evaluated using the Brunauer-Emmett-Teller (BET) and Barrett-Joyner-Halenda (BJH) methods, while X-ray photoelectron spectroscopy (XPS) was used to analyze the surface elemental composition and chemical states. Additionally, UV-visible spectroscopy (UV-vis) and photoluminescence (PL) spectra were used to examine the optical properties of the nanofibers, offering valuable insights into their electronic structure and bandgap.

2.4. Electrochemical battery cell evaluation

The electrode was prepared by mixing the active material, conductive agent, and binder in a weight ratio of 8:1:1. After heat treatment, the nf–(c)–MCO was pulverized using a Thinky mixer and then combined with the conductive agent (C.B) and binder to achieve the desired concentration. The resulting mixture was coated onto copper foil using a doctor blade and dried in a vacuum oven at 150 °C for 2 h. The electrochemical properties of the anode material, specifically nf-(c)-MCO,

were assessed through cyclic voltammetry (CV) and galvanostatic charge–discharge (GCD) experiments, which were performed using a standard 2032 coin cell configuration. The study used working electrodes with a lithium foil counter electrode, and a separator soaked in electrolyte was used to prevent direct contact between the electrodes. The electrolyte solution consisted of 1.3 M LiPF₆ dissolved in a solvent mixture of EC and DEC in a 3:7 volume ratio. Additionally, the electrolyte was enhanced with a 10 wt% concentration of FEC as an additive. The electrochemical performance of the nf–(c)–MCO electrode was evaluated using CV in a voltage range of 0.005–3 V relative to the Li/Li⁺ reference electrode at a scan rate of 0.1 mV s⁻¹. GCD measurements were performed at a constant current density of 500 mA g⁻¹ in the same voltage range of 0.005–3 V. Prior to the GCD tests, the electrode material underwent formation cycles at a lower current density of 50 mA g⁻¹ to activate it. The long-term cycling performance and capacity retention of

the Mn-doped Co_3O_4 were evaluated by subjecting the material to extended charge–discharge cycles.

3. Results and discussion

3.1. Effect of Mn-doping engineering on characteristics of nf-(c)-MCO

We aimed to incorporate Mn doping into the Co_3O_4 crystal structure by considering several key factors, thereby considerably enhancing the overall efficiency of LIBs, particularly in terms of rate performance. Fig. 1a shows a schematic illustration demonstrating how Mn doping promotes the reduction of Co_3O_4 grain size in the one–dimensional (1D) nanofibrous Mn–doped Co_3O_4 anode materials (nf–(c)–MCO), where "c" is the at.% of Mn dopants, optimized at 0.05, 0.1, and 0.2 at.%, corresponding to c values of 1, 2, and 4, respectively. The 1D architectures

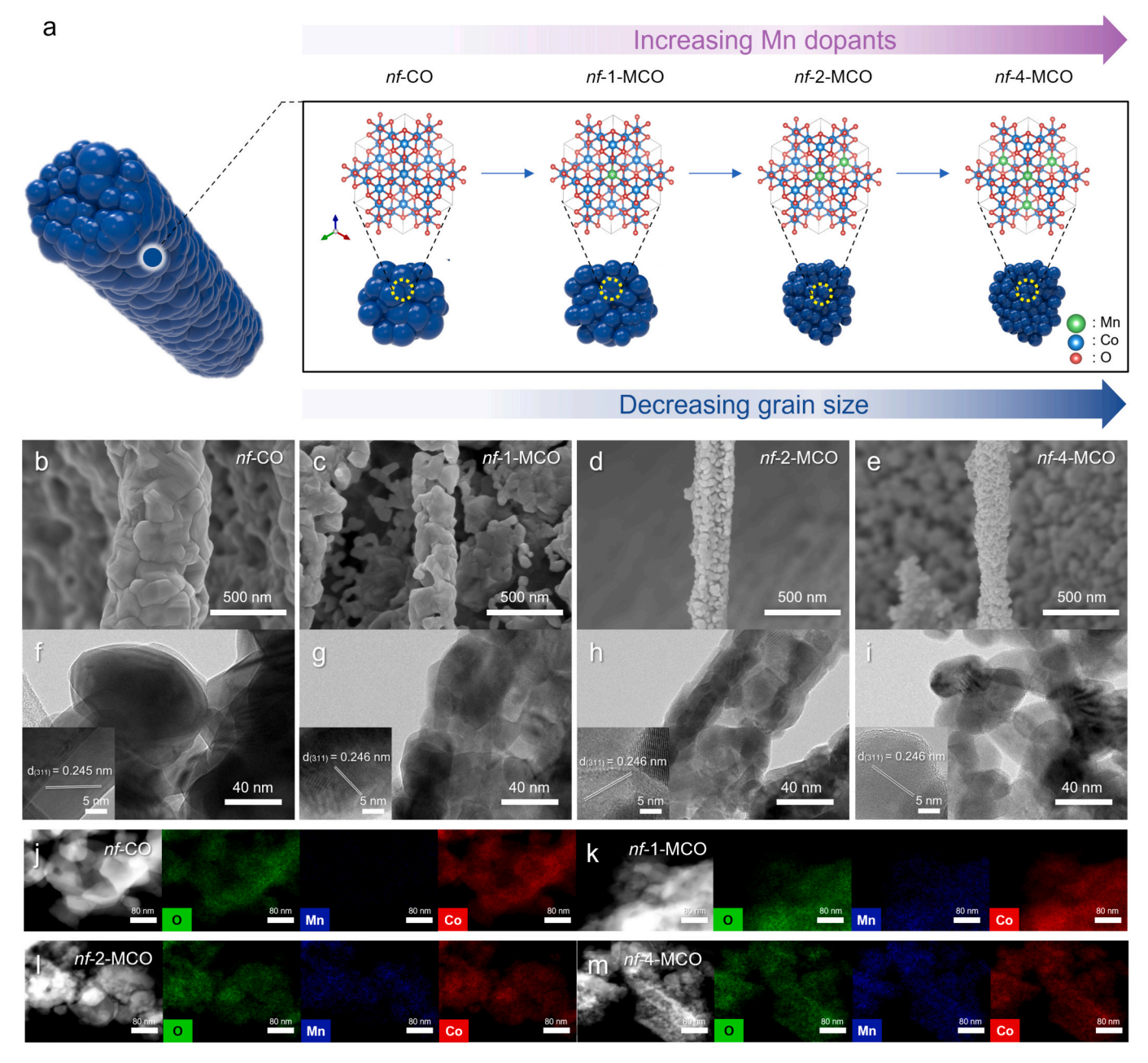


Fig. 1. (a) Schematic illustration showing the effects of Mn doping on the reduction of Co_3O_4 grain size in nf-(c)-MCO. SEM and TEM images of 1D nf-(c)-MCO: (b, f) nf-CO without Mn doping, (c, g) nf-1-MCO, (d, h) nf-2-MCO, and (e, i) nf-4-MCO. STEM-EDS elemental mapping of (j) nf-CO, (k) nf-1-MCO, (l) nf-2-MCO, and (m) nf-4-MCO.

were fabricated using the electrostatic energy–driven spinning (e-spinning) method, consisting of interconnected nf–(c)–MCO polycrystalline particles. SEM was used to examine the morphological changes in nf–(c)–MCO as Mn dopants increased, revealing a decrease in particle size with higher Mn content (Fig. 1b–e). To further investigate the unique characteristics, TEM analysis was performed on both nf–CO and nf–(c)–MCO (Fig. 1f–i). For the bare nf–CO, the average particle size of Co₃O₄ was found to be approximately 82 nm.

The inset in the HR-TEM image shows the lattice fringe with a dspacing of 0.245 nm, corresponding to the (311) crystal planes of Co₃O₄. For the other nf-(c)-MCO samples, the (311) crystal planes were observed with a d-spacing of 0.246 nm. This indicates that the Mndopant slightly increases the d-spacing interval, suggesting that Co ions are being replaced by larger Mn ions. Additionally, the nf-(c)-MCO particles appear to have downsized with increasing Mn doping, with average particle sizes of 33, 28, and 24 nm for nf-1-MCO, nf-2-MCO, and *nf*–4–MCO, respectively. The detailed differences in polycrystalline particle size are shown in Fig. S3; as the Mn doping concentration increases, the surface of the nanofiber evolves from nf-1-MCO to nf-4-MCO, leading to considerable changes in grain distribution and size. Scanning TEM (STEM) and energy-dispersive X-ray spectroscopy (EDS) elemental mappings clearly show the reduction in nanoparticle size from nf-CO to nf-4-MCO (Fig. 1j-m). The STEM-EDS mapping analysis allows for the visualization of the spatial distribution and size. Scanning TEM (STEM) and energy-dispersive X-ray spectroscopy (EDS) elemental mappings clearly show the reduction in nanoparticle size from nf-CO to nf-4-MCO (Fig. 1j-m). The STEM-EDS mapping analysis allows for the visualization of the spatial distribution of Co, O, and Mn in the nanofibers. The STEM-EDS mapping analysis provides a clearer understanding of how Mn is incorporated into the nanofiber structure. The reduction in grain size observed in the Mn-doped nf-(c)-MCO variants is a key outcome, which is expected to considerably enhance the transport of Li⁺ ions and electrons through the host structure, thereby improving overall battery performance.

3.2. Physicochemical states of nf-(c)-MCO and induced characteristics

To thoroughly investigate the crystal structures of nf–CO and nf–(c)–MCO materials, XRD analysis was performed (Fig. 2a), confirming the successful synthesis of Co_3O_4 nanofibers doped with Mn atoms and cations. The synthesized nf–CO exhibited XRD peaks at 37° and 65°, which correspond to the (311) and (440) planes, respectively, of the

cubic phase of $\rm Co_3O_4$ with a space group of Fd3m (JCPDS#42–1467). For $\it nf$ –(c)–MCO, the XRD peak positions remained unchanged, indicating that the Mn doping did not change the fundamental $\rm Co_3O_4$ crystal structure. The detailed crystal structural information is provided in Table 1. The increase in d-spacing observed in Fig. 1f–i, which aligns closely with the calculated values in Table 1, demonstrates a clear expansion of the d-spacing. The magnified XRD results in Fig. 2b reveal a shift of the peak from approximately 37° to the left as the manganese content increases. According to Bragg's law, Mn doping leads to an increase in interplanar spacing (d-spacing) because the ionic radii of Mn³⁺ (0.73 Å) and Mn²⁺ (0.82 Å) are larger than those of $\rm Co^{3+}$ (0.63 Å) and $\rm Co^{2+}$ (0.72 Å). The decrease in peak intensity with increasing Mn doping indicates a reduction in crystallinity.

These XRD data enable the calculation of the average size of crystalline particles using Scherrer's equation, providing valuable insights into the structural integrity of the nanofibers [20].

Bragg's law:

$$n\lambda = 2d\sin\theta \tag{1}$$

Scherrer's equation:

$$D = \frac{K\lambda}{\beta \cos \theta} \tag{2}$$

As observed in Fig. 2c, the full width at half maximum (FWHM) of the peaks widens with increasing Mn content. According to the Scherrer equation, an increase in FWHM corresponds to a reduction in crystallite size. This indicates that the introduction of Mn impedes crystal growth, resulting in a decrease in the average particle size of the nf–(c)–MCO. The reduction in grain size suggests an increase in surface area and improved electrode–electrolyte interaction, both crucial factors for battery performance. The doping of Mn ions may lead to structural

Table 1 Structural parameters and XRD characterization of nf-CO and nf-(c)-MCO at different doping levels.

Sample	(hkl)	Lattice parameter (Á)	d-Spacing (Á)	FWHM (°)	Crystallite size D (Å)
nf-CO	(311)	8.08218	2.44687	0.141	620.6
nf-1-MCO	(311)	8.10396	2.45544	0.304	287.5
nf-2-MCO	(311)	8.10459	2.45563	0.468	187.0
nf-4-MCO	(311)	8.10459	2.45563	0.723	121.0

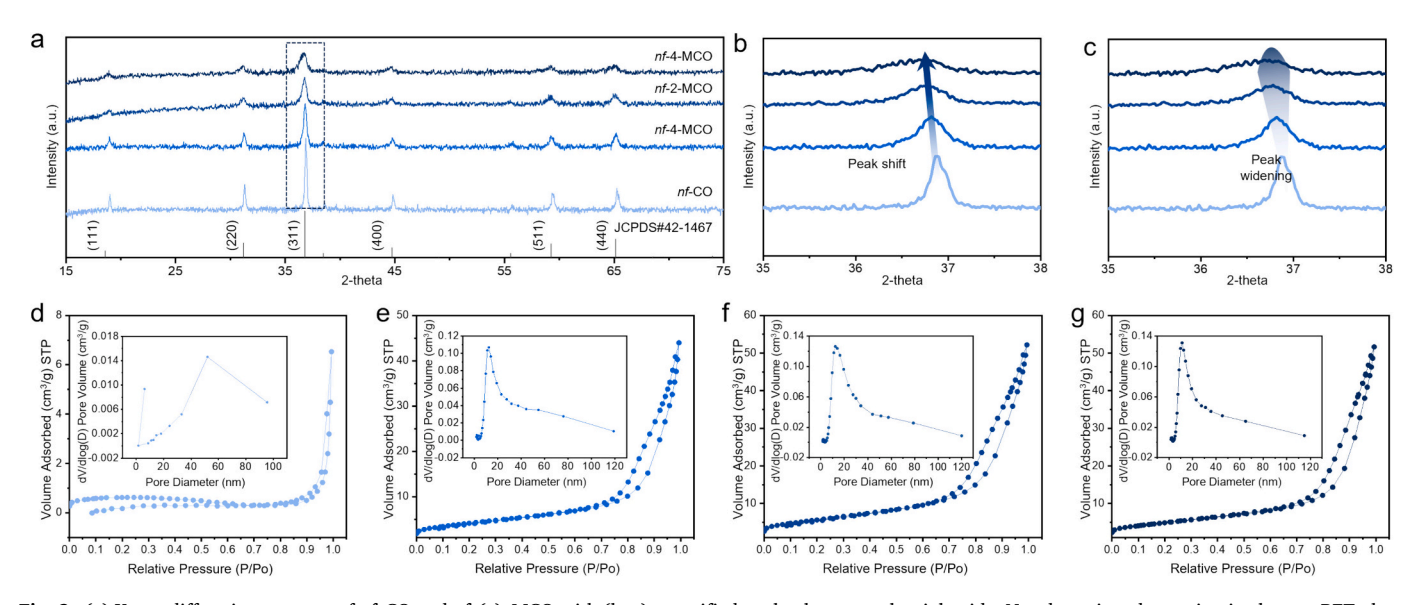


Fig. 2. (a) X-ray diffraction patterns of nf-CO and nf-(c)-MCO with (b, c) magnified peaks shown on the right side. N_2 adsorption-desorption isotherms, BET plots, and BJH pore size distribution curves for (d) nf-CO, (e) nf-1-MCO, (f) nf-2-MCO, and (g) nf-4-MCO.

expansion, facilitating enhanced ion diffusion in the electrode material and ultimately improving electrochemical performance. BET and BJH analyses were performed to evaluate the specific surface area and pore size distribution of nf–(c)–MCO (Fig. 2d–g). The surface area and porosity characteristics of the nf–(c)–MCO microstructure were calculated using the BET equation derived from N_2 adsorption–desorption isotherms [21].

The nf-CO and nf-(c)–MCO exhibited typical IV–type isotherms with hysteresis loops in the relative pressure range (P/P₀) of 0.4–1.0, confirming the mesoporous nature of the structure.

The average pore size was calculated using the BJH equation, with the corresponding values listed in Table 2.

With the introduction of Mn into Co₃O₄, the surface area considerably increased from 2.3052 m²/g for nf-CO to 15.0830 m²/g for nf-1-MCO as the Mn-dopant concentration slightly. The average pore size was calculated using the BJH equation, with the corresponding values listed in Table 2. With the introduction of Mn into Co₃O₄, the surface area considerably increased from 2.3052 m²/g for nf-CO to 15.0830 m²/g for nf-1-MCO as the Mn-dopant concentration slightly increased. As more Mn was incorporated, the specific surface area further increased, reaching 17.7056 m²/g for nf-2-MCO and 20.5919 m^2/g for nf-4-MCO. This increase likely resulted from the reduction in MCO particle size. The average pore size decreased substantially from 48.99 nm for nf-CO to 15.78, 16.32, and 13.60 nm for nf-1-MCO, nf-2-MCO, and nf-4-MCO, respectively. The nf-4-MCO, with the highest Mn doping, exhibited the largest pore volume of 0.080718 cm³/g, surpassing nf-CO (0.009833 cm³/g), nf-1-MCO (0.067975 cm³/g), and nf-2-MCO (0.080121 cm³/g). Notably, the high Mn-doped MCO (>0.2 at.%) displayed a considerable increase in pore volume. These mesoporous properties align with the findings from SEM and TEM analyses. The abundant pores in nf-4-MCO contribute to reduced electrode tortuosity and improved electrolyte accessibility, facilitating efficient Li+ ion diffusion and enhancing the (dis)charging performance.

X-ray photoelectron spectroscopy (XPS) was used to examine the oxidation states of cations and the oxygen vacancy in both nf-CO and nf-(c)-MCO with varying Mn doping levels (Fig. 3a-d). The atomic percentages (at.%) of the cations are summarized in Table 3. As the Mn doping increased, the concentration of $\rm Mn^{3+}$ and $\rm Mn^{4+}$ species also increased (Fig. 3a). The increase in the $\rm Co^{2+}/\rm Co^{3+}$ ratio indicates the reduction of Co³⁺ ions to Co²⁺, which results in the formation of new oxygen vacancies. These vacancies introduce new bonding states in the Co₃O₄ band gap. The two electrons associated with the oxygen vacancy defects can be readily excited into the conduction band, thereby improving electrical conductivity [22]. The XPS fitting analysis revealed the Co 2p core-level spectrum for all the samples, which displayed three components: Co^{3+} (approximately 779.6 eV), Co^{2+} (approximately 781.3 eV), and satellite peaks (Fig. 3b). The observed peak shift in Co 2p binding energy suggests the formation of oxygen vacancies [23]. The $\text{Co}^{2+}/\text{Co}^{3+}$ ratio for *nf*–CO was 43.78 %, while it increased to 63.60 % in nf-4-MCO, which had the highest Mn-doping level. In the spinel Co₃O₄ crystal structure, Co³⁺ and Co²⁺ cations occupy octahedral and tetrahedral sites, respectively [24]. Therefore, the increase in the Co²⁺/Co³⁺ ratio indicates that Mn dopants are replacing Co3+ at the octahedral sites. When Co³⁺ is substituted by Mn³⁺ in the octahedral sites, the four 3d-electrons in Mn³⁺ tend to be unpaired, resulting in the electronic configuration Mn^{3+} ($t_{2g}^3-e_{g}^1$). This electronic configuration results in one electron in the two degenerate e_g orbitals, differing from Co^{3+} ($t_{2g}^6 - e_g^0$).

Table 2 Pore volume, pore size, and specific surface area of *nf*-CO and *nf*-(c)-MCO.

Samples	Pore volume	Pore size	Specific surface area
nf-CO	0.009833 cm ² /g	48.9872 nm	2.3052 m ² /g
nf-1-MCO	0.067975 cm ² /g	15.7772 nm	15.0830 m ² /g
nf-2-MCO	$0.080121 \text{ cm}^2/\text{g}$	16.3166 nm	17.7056 m ² /g
nf-4-MCO	$0.080718 \text{ cm}^2/\text{g}$	13.6003 nm	$20.5919 \text{ m}^2/\text{g}$

As a result, the elongation of Mn-O bonds induced by degeneracy lifting occurs in the octahedral Mn³⁺—O₆ structure, leading to a lower overall energy [25]. The increased Mn—O bond length along the c-axis can weaken the chemical bonds to neighboring oxygen atoms, promoting the formation of oxygen vacancies near the Mn-doped sites, as evidenced in the O 1s XPS spectrum (Fig. 3c). Introducing an appropriate amount of Mn into Co₃O₄ facilitates the formation of crystal defects, such as oxygen vacancies, which in turn promotes the reduction of Co³⁺ to Co²⁺. The presence of Co²⁺ can create surface charge imbalances and facilitate the migration of other metallic species from a lower to a higher oxidation state [26]. The Mn³⁺/Mn ratio in the XPS Mn 2p peak is highest in nf-2-MCO, showing an inverse trend compared to the ratios of surface Mn²⁺/Mn and Mn⁴⁺/Mn (Fig. 3d). Notably, these results align with the trends observed in the Co³⁺/Co ratio, suggesting the substitution of Mn³⁺ for Co³⁺. The XPS spectrum of O 1s further reveals the chemical states of oxygen, including O²⁻ lattice oxygen (O₁), O⁻ at defect sites (O2) and physiosorbed oxygen (O3). However, O3 is excluded from consideration. To assess oxygen vacancies in the samples, the area ratios (O₁/O and O₂/O) of lattice oxygen to oxygen vacancies were calculated for each sample. The results show that O₁ decreased and O₂ increased as Mn dopants increased in the nf-CO, nf-1-MCO, and nf-2-MCO. Conversely, the O₁ and O₂ formation behaviors of nf-4-MCO exhibited opposite tendencies. The transport of Li⁺ can also be enhanced through electrostatically unbalanced defective sites, which possess partially positive and negative charges. For instance, Li⁺ ions are attracted to the negatively charged positions around these defects. Changes and optimization in the percentages of oxygen defects (O1/O (%) and O2/O (%)) indicate improved properties related to ion transport. The impact of the defective sites introduced by Mn doping on the electrochemical battery performance will be discussed in detail in the following section.

In addition to enhancing Li⁺ transport, the defective sites facilitate faster electron transfer because electrons in these defective states can be easily excited, thereby improving conductivity. Fig. 3e shows the calculated band gaps (E_g) of nf–CO to nf–(c)–MCO, with the optical properties evaluated through ultraviolet–visible (UV–vis) and photoluminescence (PL) spectroscopy, supported by Figs. S2–S4. The optical characteristics of the synthesized materials provide insights into impurities and energy band structures. Broad absorption peaks were observed for all samples between 400–600 and 700–800 nm. The presence of two peaks in each sample suggests the existence of two different oxidation states of cobalt cations, as well as the transition processes from O^{2-} to Co^{2+} and Co^{3+} . The E_g values were determined using the Tauc plot method based on the UV–vis spectra [27].

$$(\alpha \bullet h\nu)^{1/\gamma} = B(h\nu - E_{\sigma}) \tag{3}$$

The α represents the absorption coefficient, ho denotes the photon energy, E_g is the band gap of the synthesized material, and the γ factor indicates the type of electron or optical transition, which can take values of 1/2, 2, 3/2, or 3. When $\gamma = 1/2$, the transition is a direct allowed transition; when $\gamma = 3/2$, it corresponds to a direct forbidden transition; $\gamma = 2$ signifies an indirect allowed transition; and $\gamma = 3$ indicates an indirect forbidden transition. For the samples, the transitions were calculated as direct allowed transitions. The calculated E_{σ} values were 1.59/2.18 eV for nf-CO, 1.48/1.94 eV for nf-1-MCO, 1.44/1.89 eV for nf-2-MCO, and 1.39/1.83 eV for nf-4-MCO, respectively. It was observed that E_g decreased as the Mn doping content increased (Fig. 3f). This variation in the band gap is typically attributed to factors such as quantum confinement, crystallite size, charged impurities at grain boundaries, and structural disorder. The incorporation of Mn as an impurity into the matrix can create impurity energy levels or reduce the crystallite size, which weakens the overall crystallization. As a result, this effect promotes improved Li⁺ mobility in the electrode, thereby influencing the charging and discharging rates. In addition, the improvement in battery performance can be attributed to the slight

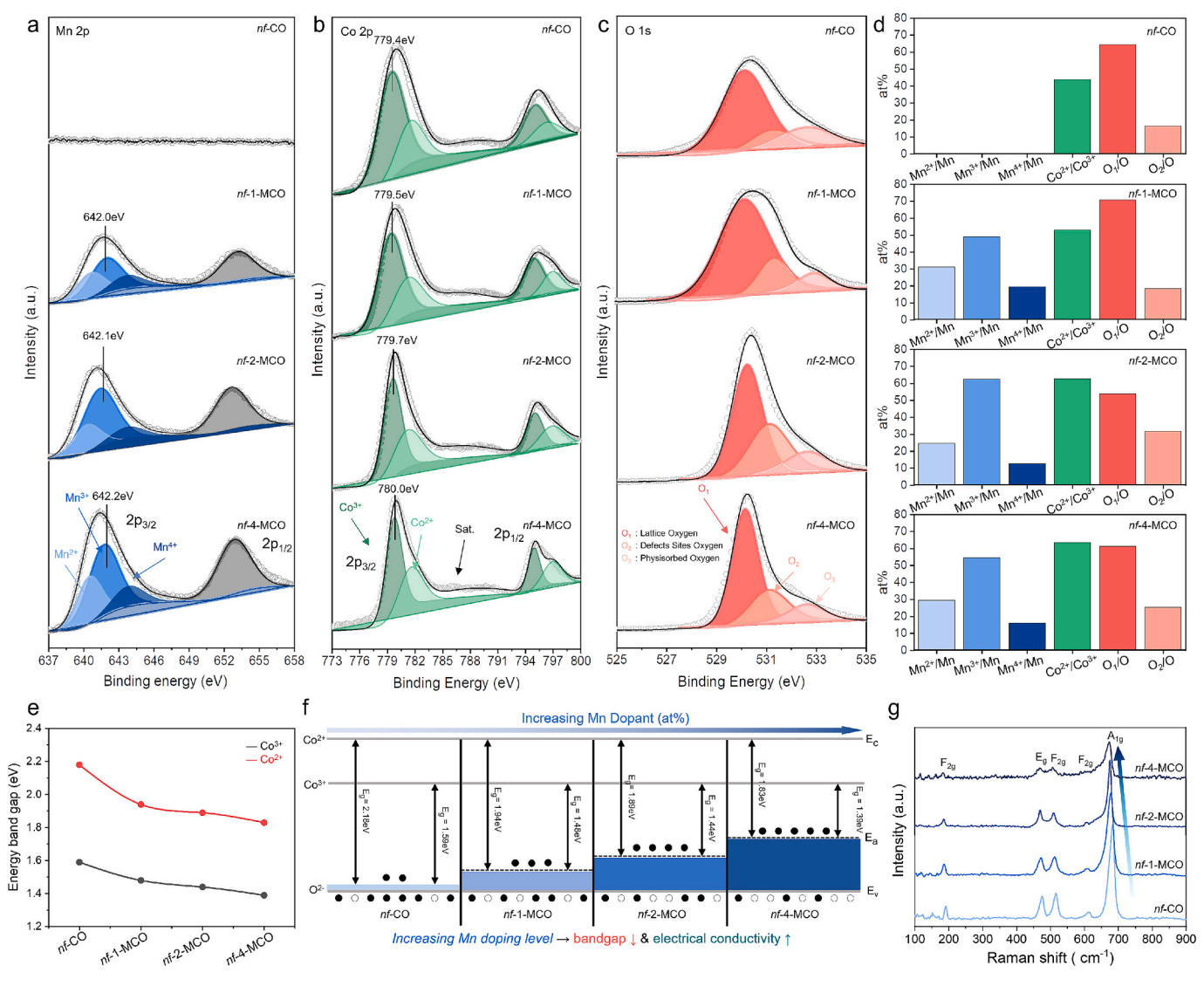


Fig. 3. X-ray photoelectron spectroscopy (XPS) analysis for nf-CO and nf-(c)-MCO. Core XPS spectra for (a) Mn 2p, (b) Co 2p and (c) O 1s. (d) Atomic percentages (at.%) derived from the XPS results for nf-CO and nf-(c)-MCO, illustrating the effects of Mn doping on elemental ratios and oxidation states. (e) Band gaps (eV) and (f) band gap diagrams for nf-CO and nf-(c)-MCO. (g) Raman spectra for nf-CO and nf-(c)-MCO.

Table 3XPS data for at.% of *nf-*CO and *nf-*(c)-MCO at different Mn-doping levels.

Samples	Mn ²⁺ /Mn	Mn ³⁺ /Mn	Mn ⁴⁺ /Mn	$\mathrm{Co}^{2+}/\mathrm{Co}^{3+}$	O ₁ /O	02/0
nf-CO	-	-	-	43.78 %	68.28 %	16.55 %
nf-1-MCO	31.28 %	49.16 %	19.57 %	53.08 %	65.12 %	18.48 %
nf-2-MCO	24.69 %	62.49 %	12.82 %	62.56 %	56.22 %	31.82 %
nf-4-MCO	29.47 %	54.52 %	16.01 %	63.60 %	62.41 %	25.42 %

expansion in crystal lattice d-spacing caused by the larger ionic radius of Mn ions, as shown in Table 1 and Fig. 2. The Raman spectra of the oxides, shown in Fig. 3g, exhibit five bands corresponding to the three active vibrational modes of the spinel structure: the F_{2g} mode for the first, third, and fourth peaks, the E_g mode for the second peak, and the A_{1g} mode for the fifth peak. As the Mn content increases, a notable decrease in peak intensity occurs, accompanied by a redshift. Specifically, when Co ions are replaced by Mn ions, the A_{1g} mode, which is associated with the octahedral cation sites, shifts to a lower wavenumber. This shift results from lattice distortions caused by Mn doping in Co_3O_4 , leading to reduced crystallinity and smaller particle sizes [28].

3.3. Electrochemical assessment of nf-(c)-MCO electrodes in LIB cells

To examine how the particle size-controlled nf-(c)-MCO could enhance battery performance, we evaluated LIB cells with nf-(c)-MCO electrodes (Fig. 4). GCD voltage profiles were obtained at a current density of 50 mA g⁻¹ for the initial cycle (Fig. 4a). The discharge capacity of nf-CO was 1025.24 mAh g⁻¹, whereas the nf-1, nf-2, and nf-4-MCO samples exhibited specific discharge capacities of 1367.65, 1101.06, and 1478.31 mAh g $^{-1}$, respectively. The corresponding charge capacities were 691.98 mAh g $^{-1}$ for \it{nf} -CO and 1033.89 mAh g $^{-1}$ for nf-1, nf-2, and nf-4-MCO. The Coulombic efficiencies were 67.49 % for nf-CO, 75.60 % for nf-1-MCO, 69.59 % for nf-2-MCO, and 71.60 % for nf-4-MCO, respectively. The lower Coulombic efficiency suggests that irreversible capacity loss may occur owing to the formation of the solidelectrolyte interphase (SEI) film, which results from irreversible reactions during the first discharge cycle. The rate capabilities of nf-CO and nf-(1,2,4)-MCO were assessed at various current densities of 0.1, 0.2, 0.5, 1.0, 3.0, and 5.0 A g^{-1} (Fig. 4b). Although nf-1--MCO showed the highest specific capacity up to 1.0 A g⁻¹, its performance declined rapidly at higher current densities of 3.0 and 5.0 A g⁻¹. When comparing the nf-2-MCO and nf-4-MCO, the nf-4-MCO exhibits a larger capacity

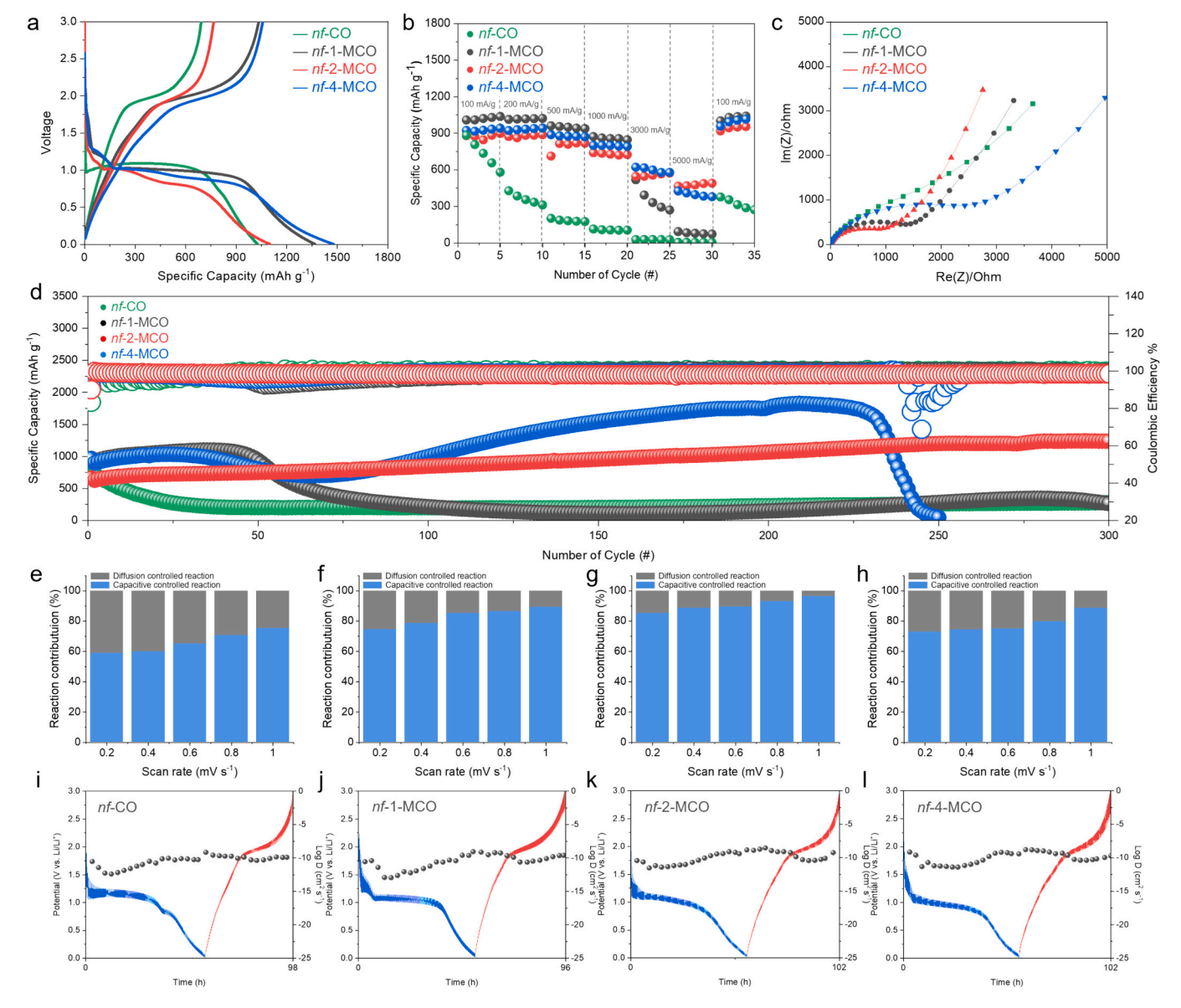


Fig. 4. Electrochemical performance of LIB cells with nf-CO and nf-(c)-MCO electrodes. (a) Galvanostatic charge–discharge voltage profiles at a current density of 50 mA g⁻¹ for the first cycle. (b) Rate capabilities evaluated at various current densities. (c) Electrochemical impedance spectroscopy (EIS) plots obtained before cycling. (d) Long-term cycling performance at 0.5 A g⁻¹. Diffusion-limited and capacitive contributions for (e) nf-CO, (f) nf-1-MCO, (g) nf-2-MCO, and (h) nf-4-MCO. Galvanostatic intermittent titration technique (GITT) curves for (i) nf-CO, (j) nf-1-MCO, (k) nf-2-MCO, and (l) nf-4-MCO, measured at a current density of 50 mA g⁻¹.

of 0.1–1.0 A g $^{-1}$, and the reduction rate of capacity between them is similar. However, at 3.0 A g $^{-1}$, nf-2-MCO exhibits less capacity fading than nf-4–MCO and maintains a higher capacity even at 5.0 A g $^{-1}$. nf-2–MCO demonstrates the best rate capability, even at high current densities, suggesting that there is an optimal level of Mn doping in the nf-(c)-MCO for Li $^+$ reactions.

To further investigate how the material properties contribute to the fast (dis)charging ability, electrochemical impedance spectroscopy (EIS) measurements were performed before and after the 1st, 50th, and 100th cycles (Figs. 4c and S5). The equivalent circuit used for EIS is shown in Fig. S8. The semicircle at high frequency corresponds to the charge-transfer process, while the low-frequency region reflects the Li⁺ ion diffusion process. R_s represents the solution resistance of the electrolyte, R_{ct} is the charge-transfer resistance, C is the double-layer capacitance, and W denotes the Warburg impedance. The Li⁺ ion diffusion coefficient (D_{Li+}) can be calculated from the low-frequency part of the Nyquist plots. The charge–transfer resistance values before cycling for nf–CO,

nf-1–MCO, nf-2–MCO, and nf-4–MCO were 2623.1, 1251.5, 900, and 2355 Ω , respectively.

The EIS results obtained after cycling reveal the charge-transfer resistance (R_{ct}) and lithium diffusion coefficient ($D_{\rm Li+}$) for various electrode formulations over multiple cycles. For $\it nf$ –CO, the R_{ct} values after 1, 50, and 100 cycles are 101.11, 140.44, and 177.45 Ω , respectively, with corresponding $D_{\rm Li+}$ values of 9.40 \times 10 $^{-12}$, 1.13 \times 10 $^{-13}$, and 3.65 \times 10 $^{-13}$ cm 2 s $^{-1}$. For $\it nf$ -1-MCO, the R_{ct} values are 83.55, 120.12, and 140.55 Ω , respectively, while the $D_{\rm Li+}$ values are 6.95 \times 10 $^{-11}$, 8.89 \times 10 $^{-11}$, and 1.02 \times 10 $^{-12}$ cm 2 s $^{-1}$. The $\it nf$ -2-MCO shows R_{ct} values of 66.60, 79.93, and 85.71 Ω over the same cycles, with corresponding $D_{\rm Li+}$ values of 9.87 \times 10 $^{-10}$, 1.25 \times 10 $^{-11}$, and 4.9 \times 10 $^{-11}$ cm 2 s $^{-1}$. In comparison, $\it nf$ -4-MCO records R_{ct} values of 101.42, 138.22, and 168.24 Ω , with $D_{\rm Li+}$ values of 1.07 \times 10 $^{-11}$, 4.51 \times 10 $^{-11}$, and 8.90 \times 10 $^{-11}$ cm 2 s $^{-1}$. Before cycling, the R_{ct} values follow the order $\it nf$ -2-MCO < $\it nf$ -1-MCO < $\it nf$ -4-MCO, exhibit enhanced

conductivity. This suggests that nf-2-MCO is likely to facilitate the fastest charge-transfer reactions during the charge/discharge process. The post-cycle EIS data reveal a general reduction in resistance, indicating electrode activation and the formation of a stable SEI that enhances charge transfer. After cycling, the lowest resistance values are observed in nf-2-MCO, followed by nf-1-MCO, nf-4-MCO, and nf-CO in ascending order. Additionally, nf-2-MCO exhibits the smallest increase in resistance with cycling, suggesting superior retention and conductivity. Regarding lithium diffusion coefficients, the order from highest to lowest is nf-2-MCO > nf-4-MCO > nf-1-MCO > nf-CO, with nf-2-MCO demonstrating the highest Li⁺ diffusion coefficients. Fig. 4d shows the long-cycle performance evaluation of *nf*–CO and *nf*–(c)–MCO at a high current density of 0.5 A g⁻¹. The specific discharge capacities of nf-(c)-MCO are considerably higher than those of bare Co₃O₄ without Mn doping. For nf-CO, the initial coulombic efficiency is 83.31 %. A substantial irreversible capacity loss is observed during the first cycle, after which the coulombic efficiency remains at 95 % until the capacity decreases to 200 mAh g⁻¹. From that point, the capacity is stabilized with a coulombic efficiency (CE) close to 100 % at 200 mAh g⁻¹. The rapid capacity fading observed in nf-CO is likely attributed to considerable volume expansion during the fast alternation between charging and discharging processes. The nf-1-MCO electrode demonstrates an initial discharge capacity of 969.06 mAh g⁻¹ and a charge capacity of 920.22 mAh g⁻¹, resulting in a CE of 94.96 %. Compared to nf-CO, nf-1-MCO exhibits a smaller irreversible capacity loss during the first cycle, with subsequent CEs approaching 100 %. While the specific discharge capacity initially increases, it begins to decrease sharply after the 41st cycle, reaching 166.38 mAh g⁻¹ by the 180th cycle. Afterward, the capacity remains relatively stable. The capacity retention from the first cycle (969.06 mAh g^{-1}) to the 300th cycle (271.02 mAh g^{-1}) is only 27.97 %, indicating a considerable loss in capacity. In contrast, the nf–2–MCO exhibits a first-cycle discharge capacity of 662.09 mAh g $^{-1}$ and a charge capacity of 595.64 mAh $\rm g^{-1}$, resulting in a CE of 89.96 %. After the initial cycle, excellent Coulombic efficiencies close to 100 % are maintained. A steady increase in non-dischargeable capacity is observed, with a capacity of 1237.76 mAh g⁻¹ at the 300th cycle. This capacity increase is typically attributed to the reversible growth of a polymeric gel-like film on the electrode surface [29]. Because these films exhibit pseudocapacitive properties, the observed increase in capacity can be explained. This rapid capacity fading can be attributed to structural instability caused by excessive Mn doping. The high concentration of Mn leads to over-shrinking of Co₃O₄ nanograins and induces significant lattice strain, as a large number of relatively larger Mn ions substitute for smaller Co ions. This strain likely results in microstructural degradation during repeated cycling, ultimately leading to premature cell failure. Fig. 4(e-h) show the Li⁺ storage mechanism (diffusion- or capacitive-controlled reactions) for the nf-CO and nf-(c)-MCO electrodes. CV tests were performed on each sample at scan rates of 0.2, 0.4, 0.6, 0.8, and 1.0 mV s^{-1} (Fig. S9). At the 1.0 mV s^{-1} scan rate used as a reference, the nf-CO exhibits a pseudocapacitive energy storage contribution of 75.35 %. In comparison, nf-1-MCO, nf-2-MCO, and nf-4-MCO show capacitive-controlled reaction behaviors of 89.45 %, 96.56 %, and 88.53 %, respectively. This indicates that nf-2-MCO demonstrates the highest pseudocapacitive characteristics owing to its optimal interfaces that support electric double layers. This trend in electrochemical behavior also aligns with variations in oxygen vacancies. These vacancies are crucial for enhancing ionic and electronic transport by narrowing the bandgap of nf-(c)-MCO, which in turn increases electrochemical conductivity and improves the pseudo-capacity characteristics [8,30]. Moreover, the complex structure with a larger surface area and enhanced electrical conductivity, facilitated by the 1D nanofiber building blocks, improves Li+ transport kinetics, leading to enhanced pseudo-capacity [31]. Evidence supporting pseudo-capacitor characteristics can be seen in the changes in galvanostatic discharge-charge behavior with Mn doping, as shown in Fig. S10. The nf-2-MCO displays the most linear graph, demonstrating the highest

pseudo-capacitor characteristics. This indicates abundant surfaceadsorbed electrons owing to "downsizing and electrostatic unbalance effects," resulting in a higher capacity than the theoretical capacitance. This phenomenon helps explain why the observed capacity exceeds the initial value. The capacitive-controlled responses are most dominant in nf-CO, nf-1-MCO, and nf-2-MCO, as shown in Fig. 4(e-g). In contrast, nf-(4)-MCO exhibits an opposite trend (Fig. 4h). The decline in capacitive contribution for nf-(4)-MCO can be attributed to two primary factors. First, XPS analysis reveals a reduction in oxygen vacancies compared to nf-(2)-MCO, which limits the active sites available for charge storage and weakens the pseudocapacitive behavior. Second, excessive Mn doping introduces structural instability, disrupting electron transport pathways and reducing conductivity. These combined effects result in the observed decrease in pseudocapacitive characteristics for *nf*–4–MCO, highlighting the importance of optimizing Mn doping levels and maintaining sufficient oxygen vacancies for enhanced performance. To assess the fast-chargeable capability of the nf-(c)-MCO electrode, GITT was used to determine the Li^+ diffusion coefficient. GITT was performed at a current density of 50 mA g⁻¹, with a 10-min rest period and a 10-min constant current application. The Li⁺ diffusion coefficients, as shown in Fig. S11, were calculated by analyzing timedependent voltage changes, excluding the flat regions where phase transitions occur. The average Li⁺ diffusion coefficients for nf-CO, nf-1-MCO, nf-2-MCO, and nf-4-MCO were found to be 1.6443 \times 10⁻¹⁰ 3.5872×10^{-10} , 8.3681×10^{-10} , and 6.5106×10^{-10} cm² s⁻¹, respectively. The Li⁺ ion diffusion coefficients follow the order: nf-2-MCO > nf-4-MCO > nf-1-MCO > nf-CO, with nf-2-MCO showing the highest diffusion coefficient. Although the absolute values of the Li diffusion coefficients calculated by GITT and EIS differ due to the intrinsic differences in measurement principles and analysis conditions, both methods consistently indicate the same trend among the samples. GITT evaluates Li⁺ diffusivity based on transient voltage responses under near-equilibrium states, whereas EIS assesses ion transport behavior in the frequency domain, which includes interfacial effects and resistive components. Given the distinct time and frequency scales of these techniques, discrepancies in the calculated values are anticipated. Therefore, the diffusion coefficients presented in this study should be interpreted not as precise absolute values, but as comparative indicators to evaluate the relative electrochemical kinetics among the samples. When compared to nf-CO and nf-1-MCO, the nf-2-MCO and nf-4-MCO electrodes, which are adequately doped with Mn, exhibited superior Li⁺ diffusion coefficients. This enhancement can be attributed to the reduction in particle size, improved pore characteristics, increased oxygen vacancies, and a narrowed bandgap resulting from Mn doping. To further validate these findings, CV was performed at a scan rate of 0.1 mV s⁻¹ for all electrodes (Fig. S12). During the discharging process, reduction peaks appeared at 0.76, 0.80, 0.84, and 0.61 V for nf-CO, nf-1-MCO, nf-2-MCO, and nf-4-MCO, respectively. The irreversible reduction reactions observed after the first CV cycle indicate the formation of a SEI layer on the electrode surface. This SEI layer plays a crucial role in stabilizing the electrode-electrolyte interface and facilitating ion transport. Distinct redox peaks on the CV curves correspond to the reversible Li⁺ insertion and extraction reactions. After the initial formation cycle, the SEI layer forms, accompanied by an irreversible reduction reaction, which stabilizes the electrode-electrolyte interface and prevents further electrolyte decomposition. This irreversible reduction reaction is represented as follows:

"SEI Formation (irreversible reduction reaction)":

$$Co3O4 + 2Li+ + 2e- \rightarrow 2CoO + Li2O$$
 (4)

$$CoO + 2Li^{+} + 2e^{-} \rightarrow Co + Li_{2}O$$
 (5)

The SEI layer primarily consists of compounds such as lithium cobalt oxide (Li_2CoO_3), lithium oxide (Li_2O), and lithium alkyl carbonates (ROCO₂Li). This layer forms as a result of the reduction of Co_3O_4 during the initial lithiation process. Moreover, oxidation and reduction

reactions involving Co and cobalt monoxide (CoO) were observed, indicating the reversible transformation between different oxidation states of cobalt throughout the cycling process. In the second and third cycles, lithiation occurs at approximately 1.0 V, while delithiation is observed near 2.1 V. Aside from the irreversible reactions that form a stable SEI layer during the first cycle, reversible reactions dominate, as indicated by the reduction and oxidation peaks appearing at consistent voltage levels during the charge–discharge process. During the first

cycle of anode scanning, a distinct oxidation peak at 2.1 V was observed, corresponding to the phase transition of Co being oxidized to ${\rm Co}^{2+}$ and ${\rm Co}^{3+}$. This is represented in formulas (5) and (6), as follows:

$$Co + Li_2O \rightarrow CoO + 2Li^+ + 2e^-$$
 (6)

$$3\text{CoO} + \text{Li}_2\text{O} \rightarrow \text{Co}_3\text{O}_4 + \text{Li}^+ + 2\text{e}^-$$
 (7)

The lithium storage mechanism of Co_3O_4 is based on the conversion reactions as follows:

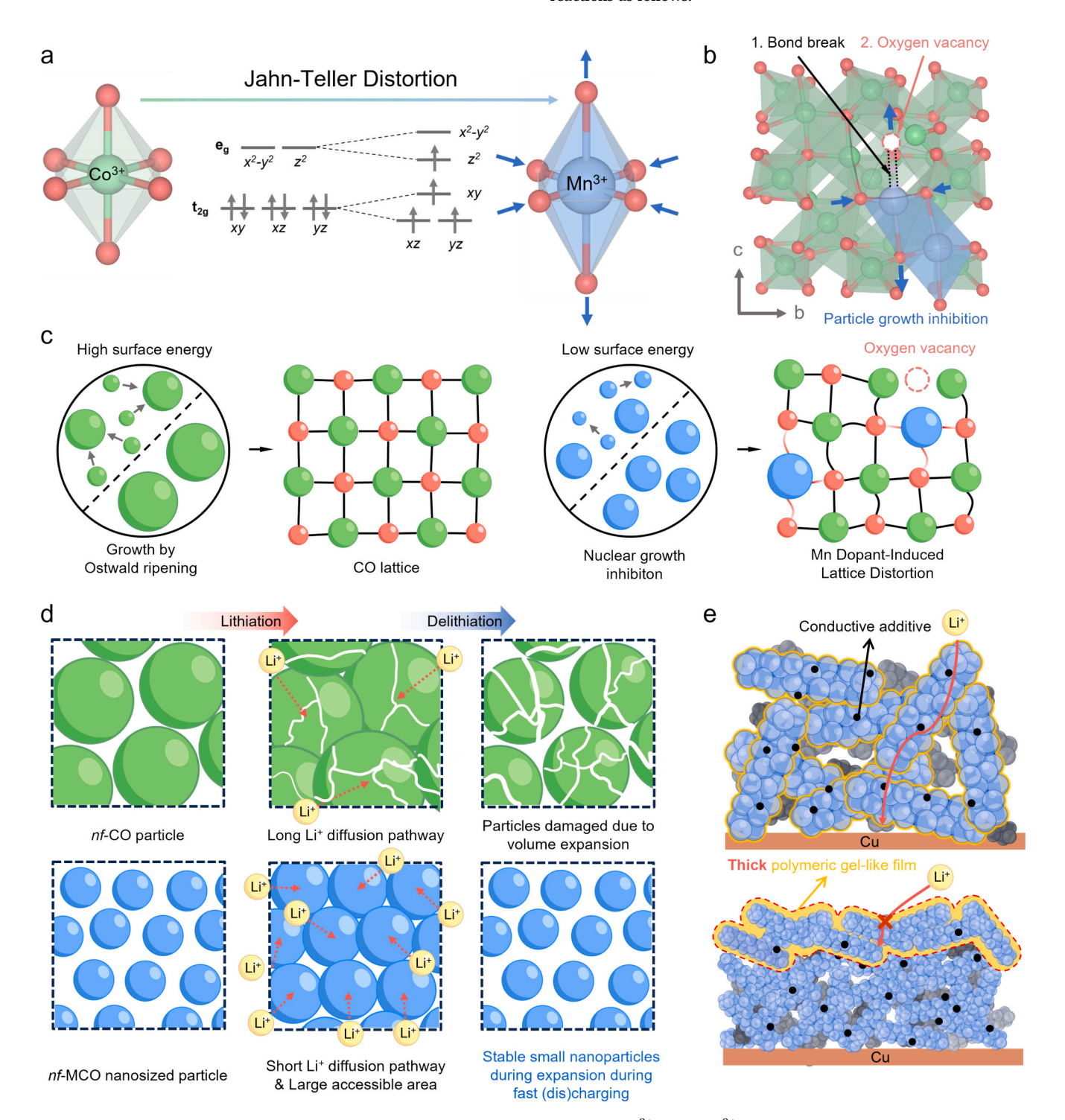


Fig. 5. (a) Schematic representation of the electronic configurations illustrating the octahedral $Co^{3+}O_6$ and $Mn^{3+}O_6$ structures, both with and without Jahn–Teller distortion. (b) Schematic depiction of the effects of Jahn–Teller distortion. (c) Schematic illustration of the mechanism for particle size reduction via doping. (d) Electrochemical reaction mechanism highlighting the dynamic roles of nf–CO and nf–(c)–MCO in lithium reactions. (e) Schematic illustration of the mechanism for the effect of particle size on a polymeric gel-like film formed on the 1D nanofibers.

$$Co_3O_4 + 8Li^+ + 8e^- \rightarrow 4Li_2O + 2Co$$
 (8)

Fig. S13 shows ex-situ SEM images of the electrodes after 0, 50, and 100 cycles from postmortem cells with nf-CO and nf-(c)-MCO electrodes. In the case of nf-CO, considerable structural degradation was observed after 100 cycles, which was attributed to repetitive and severe volume expansion of the Co₃O₄ particles. This resulted in a thick and irregular SEI layer. In contrast, the Mn-doped electrodes exhibited different behavior. After 100 cycles, these electrodes maintained their structure with minimal volume expansion. For *nf*–1–MCO, a relatively thick SEI layer was observed after 50 cycles, likely owing to the larger particle size. The *nf*-2-MCO exhibited a thin and stable SEI layer, preserving its structural integrity even after 100 cycles. In contrast, the nf-4-MCO, although forming a stable SEI layer by 50 cycles, developed a thicker SEI layer than nf-2-MCO after 100 cycles. These observations suggest that nf-2-MCO demonstrates the most optimal SEI layer formation and structural stability, which can be attributed to its particle size and well-balanced properties.

3.4. Principle of downsizing Co_3O_4 nanoparticles by Mn-doping engineering and intrinsic correlations

The mechanism behind the downsized nf-(c)-MCO is closely linked to its fast-chargeable LIB performance, as depicted in the schematic in Fig. 5. Fine lattice distortion occurs at Mn–doped sites, where Co ions are replaced by Mn ions, creating point defects. This substitution changes bond lengths and angles, further compressing the lattice. These changes are attributed to the "Jahn–Teller distortion" observed in Mn³⁺ ions with an average oxidation state lower than 3.5, leading to increased compressibility through the expansion of the octahedral coordination (Fig. 5a). The XPS analysis reveals that Mn³⁺ easily substitutes for Co³⁺ at the octahedral sites, likely owing to the Jahn-Teller distortion resulting from differences in atomic radii. This distortion elongates the bond lengths along the c-axis, which can distort the lattice structure [25]. Such distortions decrease lattice stability, weaken the bonding between oxygen atoms and surrounding metal ions, and promote the formation of oxygen vacancies (Fig. 5b). These oxygen vacancies modify the electrochemical reactivity and stability, thereby enhancing the electronic conductivity of MCO. Acting as free carriers, the vacancies increase electron concentration and improve conductivity. They also influence the band gap, making electron movement easier. While research on the reduction in particle size owing to doping is not fully conclusive, several hypotheses can be proposed (Fig. 5c).

First, manganese (II, III) oxides have lower surface energy compared to Co₃O₄ [32]. If the surface energy is low, even if the particle size decreases and the surface area increases, the overall energy increase remains minimal, making smaller particles relatively more stable. In general, for particle growth to occur, grain boundaries must migrate. However, the alteration of surface energy by Mn doping hinders grain boundary movement or reduces the driving force for particle growth, thereby stabilizing smaller particles. Co₃O₄ undergoes particle growth via an Ostwald ripening mechanism, where smaller crystallites merge to form larger ones [33]. However, Mn doping reduces surface energy, making recrystallization more difficult, thereby inhibiting particle growth and preserving smaller particle sizes. Second, the ionic radius difference owing to Mn doping causes lattice distortion, which obstructs crystal growth [34]. Third, Mn doping induces oxygen vacancies that create lattice stress, potentially blocking growth pathways or keeping nuclei smaller. Finally, the oxygen adsorption energy follows the order $Mn^{4+} > Co^{3+} > Mn^{3+} > Co^{2+} > Mn^{2+}$, and when Mn^{3+} replaces Co^{3+} , the relatively lower oxygen adsorption energy reduces reactivity, contributing to smaller particle sizes [35]. Optimized small Mn-doped Co₃O₄ particles offer several advantages in the reaction with Li⁺ ions (Fig. 5d). The relatively larger Co₃O₄ particles in the 1D nf-CO experience considerable volume changes and exhibit sluggish Li⁺ diffusion kinetics over long pathways during lithiation/delithiation. In contrast,

the reduced particle size of nf-(c)-MCO, especially nf-2-MCO, provides ample void space and accessible surface area, facilitating efficient Li+ ion transport and accommodating structural deformation during cycling by effectively dispersing stress. The smaller grains, along with an optimal concentration of oxygen vacancies, shorten the diffusion pathways for Li⁺ ions, enhancing ion conductivity and accelerating charge/ discharge rates. The optimal oxygen vacancies also create additional pathways for Li⁺ movement. Furthermore, the increased surface area of the Mn-doped MCO particles provides highly active sites, considerably enhancing electrochemical reactivity, capacity, and rate capability. The reduction in grain and crystallite sizes creates an environment with lower activation energy, thereby promoting improved charge transfer and diffusion kinetics. All these characteristics of miniaturized nf-2-MCO collectively contribute to the enhanced electrochemical performance of LIB cells [36]. In addition, there are other factors that further enhance the electrochemical performance. Co₃O₄ is fabricated in a 1D nanofiber morphology, which improves lithium mobility while mitigating volume expansion in nanofibers [37]. During repetitive discharge-charge cycling, the intrinsic correlations between material properties and battery performance can be observed, along with the gel-like film and particle size [29]. The polymeric gel-like film forms during the electrochemical reactions of metal oxides and demonstrates the ability to conduct both electrons and Li⁺ ions, unlike the SEI layers, which allow only ionic conduction. This mixed ionic-electronic conduction feature facilitates additional surface reactions, contributing surface capacity beyond the existing structural capacity and thereby increasing the total capacity. As a result, this enhances electrochemical reactions and improves the electrical performance of the electrode. However, when the particle size is too small, as seen in nf-4-MCO, excessive unwanted reactions can occur owing to the large surface area (Fig. 5e). This results in the thickening of the polymeric gel-like film, which negatively impacts electronic and ionic conductivities, ultimately reducing the overall efficiency of the battery. Thus, advanced and optimized doping engineering of Mn on Co₃O₄ is essential for controlling the smaller MCO particles to achieve improved lithium-ion battery performance in terms of both cycling stability and rate capabilities compared to their non-doped versions.

4. Conclusion

In conclusion, we investigated the effects of Mn dopants in Co₃O₄ nanofibers for lithium-ion battery anodes. The presence of Mn dopants hindered grain growth in Co_3O_4 during the sintering of nf–(c)–MCO by inducing Jahn-Teller distortion and creating oxygen vacancies in the O-Co-O lattice. Notably, the incorporation of 0.2 at.% Mn in nf-2-MCO resulted in the formation of appropriately sized MCO particles, which optimized material properties related to grain size, pore structure, and accessible area for Li⁺ ions. The nf-2-MCO demonstrated improved lithium-ion diffusion and charge transfer, leading to enhanced ionic and electronic transport. This resulted in exceptional electrochemical performance, especially evident in its remarkable rate capability, achieving a high specific capacity of approximately 500 mAh g⁻¹ at a rate of 5 A g⁻¹. Postmortem SEM and XRD analyses confirm the structural integrity and stability of the doped nanofibers, underscoring their durability and extended operational lifetime. We engaged in a thorough discussion regarding the mechanisms behind successful doping and fast-chargeable anode reactions. Our findings offer valuable insights into sustainable energy storage and establish a strong foundation for enhancing battery design and efficiency. Moreover, this approach to doping engineering demonstrates versatility, providing a pathway to optimize other materials for high-performance and sustainable energy solutions.

CRediT authorship contribution statement

Hyunmin Na: Writing – original draft, Visualization, Methodology,

Investigation, Data curation, Conceptualization. Ho-Jin Lee: Writing – original draft, Methodology, Investigation, Formal analysis. Dae-Kwon Boo: Visualization, Investigation, Formal analysis. Ilgyu Kim: Resources, Data curation. Jeong-Ho Park: Resources, Formal analysis, Data curation. Jae-Woo Seo: Investigation, Formal analysis. Seon-Jin Choi: Investigation, Formal analysis. Jiyoung Lee: Investigation, Data curation. Tae Gwang Yun: Validation, Project administration, Funding acquisition. Byungil Hwang: Project administration, Funding acquisition. Jun Young Cheong: Writing – review & editing, Supervision, Data curation, Conceptualization. Ji-Won Jung: Writing – review & editing, Writing – original draft, Supervision, Project administration, Funding acquisition, Data curation, Conceptualization.

Declaration of competing interest

The authors declare that they have no known competing financial interests or personal relationships that could have appeared to influence the work reported in this paper.

Acknowledgments

This research was supported by GRDC (Global Research Development Center) Cooperative Hub Program through the National Research Foundation of Korea (NRF) funded by the Ministry of Science and ICT (MSIT) (RS-2023-00257595). This work was supported by the National Research Foundation of Korea (NRF) grant funded by the Korea government (MSIT) (No. RS-2023-00213749).

Appendix A. Supplementary data

Supplementary data to this article can be found online at https://doi.org/10.1016/j.cej.2025.164523.

Data availability

Data will be made available on request.

References

- J. Neumann, M. Petranikova, M. Meeus, J.D. Gamarra, R. Younesi, M. Winter, S. Nowak, Recycling of lithium-ion batteries—current state of the art, circular economy, and next generation recycling, Adv. Energy Mater. 12 (2022), https://doi.org/10.1002/aenm.202102917.
- [2] N. Flores-Diaz, F. De Rossi, A. Das, M. Deepa, F. Brunetti, M. Freitag, Progress of photocapacitors, Chem. Rev. 123 (2023) 9327–9355, https://doi.org/10.1021/acs. chemrev.2c00773.
- [3] C.P. Grey, D.S. Hall, Prospects for lithium-ion batteries and beyond—a 2030 vision, Nat. Commun. 11 (2020) 2–5, https://doi.org/10.1038/s41467-020-19991-4.
- [4] S. Li, K. Wang, G. Zhang, S. Li, Y. Xu, X. Zhang, X. Zhang, S. Zheng, X. Sun, Y. Ma, Fast charging anode materials for lithium-ion batteries: current status and perspectives, Adv. Funct. Mater. 32 (2022) 1–35, https://doi.org/10.1002/ adfm.202200796.
- [5] L. Zhao, T. Wang, F. Zuo, Z. Ju, Y. Li, Q. Li, Y. Zhu, H. Li, G. Yu, A fast-charging/discharging and long-term stable artificial electrode enabled by space charge storage mechanism, Nat. Commun. 15 (2024) 1–12, https://doi.org/10.1038/s41467-024-48215-2
- [6] S.A. Han, M. Naqi, S. Kim, J.H. Kim, All-day wearable health monitoring system, EcoMat 4 (2022) 1–24, https://doi.org/10.1002/eom2.12198.
- [7] M. Weiss, R. Ruess, J. Kasnatscheew, Y. Levartovsky, N.R. Levy, P. Minnmann, L. Stolz, T. Waldmann, M. Wohlfahrt-Mehrens, D. Aurbach, M. Winter, Y. Ein-Eli, J. Janek, Fast charging of lithium-ion batteries: a review of materials aspects, Adv. Energy Mater. 11 (2021), https://doi.org/10.1002/aenm.202101126.
- [8] I.V. Thorat, D.E. Stephenson, N.A. Zacharias, K. Zaghib, J.N. Harb, D.R. Wheeler, Quantifying tortuosity in porous Li-ion battery materials, J. Power Sources 188 (2009) 592–600, https://doi.org/10.1016/j.jpowsour.2008.12.032.
- [9] Y. Zhao, Y. Fu, Y. Meng, Z. Wang, J. Liu, X. Gong, Challenges and strategies of lithium-ion mass transfer in natural graphite anode, Chem. Eng. J. 480 (2024) 148047, https://doi.org/10.1016/j.cej.2023.148047.
- [10] S. Chen, C. Liu, R. Feng, Z. Chen, Y. Lu, L. Chen, Q. Huang, Y. Guan, W. Yan, Y. Su, N. Li, F. Wu, Natural graphite anode for advanced lithium-ion batteries: challenges, progress, and perspectives, Chem. Eng. J. 503 (2025) 158116, https://doi.org/10.1016/j.cei.2024.158116.
- [11] Y. Liao, H. Zhang, Y. Peng, Y. Hu, J. Liang, Z. Gong, Y. Wei, Y. Yang, Electrolyte degradation during aging process of lithium-ion batteries: mechanisms,

- characterization, and quantitative analysis, Adv. Energy Mater. 14 (18) (2024) 1–29, https://doi.org/10.1002/aenm.202304295.
- [12] Y. Liu, H. Shi, Z.S. Wu, Recent status, key strategies and challenging perspectives of fast-charging graphite anodes for lithium-ion batteries, Energy Environ. Sci. 16 (2023) 4834–4871, https://doi.org/10.1039/d3ee02213g.
- [13] P. Jing, K. Liu, L. Soule, J. Wang, T. Li, B. Zhao, M. Liu, Engineering the architecture and oxygen deficiency of T-Nb₂O₅-carbon–graphene composite for high-rate lithium-ion batteries, Nano Energy 89 (2021) 106398, https://doi.org/ 10.1016/j.nanoen.2021.106398.
- [14] J. Liu, P. Jing, L. Zheng, N. Guo, C. Liu, H. Wang, Diffusion tunnel shortening and Oxygen-Vacancy boosting high rate and stable lithium ion storage of crystallographic self-healed Ti₂Nb₁₀O₂₉ anode, Chem. Eng. J. 482 (2024) 148866, https://doi.org/10.1016/j.cej.2024.148866.
- [15] L. Feng, S. Zhou, H. Cui, R.A. Soomro, P. Zhang, B. Xu, Multi-functional MXene binder enables ultra-stable and high-capacity Li₄Ti₅O₁₂ anode for lithium ion batteries, Energy Storage Mater. 75 (2025) 104079, https://doi.org/10.1016/j. ensm.2025.104079.
- [16] S.H. Cho, J.W. Jung, C. Kim, I.D. Kim, Rational design of 1-D $\rm Co_3O_4$ nanofibers@ low content graphene composite anode for high performance Li-ion batteries, Sci. Rep. 7 (2017) 1–9, https://doi.org/10.1038/srep45105.
- [17] A.K. Azad, A.M. Abdalla, P.I.I. Kumarasinghe, S. Nourean, A.T. Azad, J. Ma, C. Jiang, M.M.K. Dawood, B. Wei, C.N.K. Patabendige, Developments and key challenges in micro/nanostructured binary transition metal oxides for lithium-ion battery anodes, J. Energy Storage 84 (2024) 110850, https://doi.org/10.1016/j. est.2024.110850.
- [18] X. Li, Q. Chu, M. Song, C. Chen, Y. Li, X. Tian, Y. Cui, D. Zhao, Porous CoO/Co₃O₄ nanoribbons as a superior performance anode material for lithium-ion batteries, Appl. Surf. Sci. 618 (2023) 156658, https://doi.org/10.1016/j.apuse.2023.156658
- [19] Y. Zhang, M. Xie, Y. He, Y. Zhang, L. Liu, T. Hao, Y. Ma, Y. Shi, Z. Sun, N. Liu, Z. John Zhang, Hybrid NiO/ Co₂O₄ nanoflowers as high-performance anode materials for lithium-ion batteries, Chem. Eng. J. 420 (2021) 130469, https://doi.org/10.1016/j.cei.2021.130469.
- [20] Y. Cantu, A. Remes, A. Reyna, D. Martinez, J. Villarreal, H. Ramos, S. Trevino, C. Tamez, A. Martinez, T. Eubanks, J.G. Parsons, Thermodynamics, kinetics, and activation e nergy studies of the sorption of chromium(III) and chromium(VI) to a Mn₃O₄ nanomaterial, Chem. Eng. J. 254 (2014) 374–383, https://doi.org/10.1016/j.cgi.2014.05.110.
- [21] S. Kuppusamy, A.P. Veedu, A.M. Mohan, K. Rajagopalan, M. Magni, L. Gopalakrishnan, P. Deivasigamani, *Punica* grantum peel extract decorated Al-MOF scaffold as solid-state sensor/concentrator for the sensing/reduction of Cr(VI) and its extended utility as a corrosion inhibitor in Al-Air batteries, Chem. Eng. J. 496 (154070) (2024), https://doi.org/10.1016/j.cej.2024.154070.
- [22] Y. Wang, T. Zhou, K. Jiang, P. Da, Z. Peng, J. Tang, B. Kong, W. Bin Cai, Z. Yang, G. Zheng, Reduced mesoporous Co₃O₄ nanowires as efficient water oxidation electrocatalysts and supercapacitor electrodes, Adv. Energy Mater. 4 (2014) 1–7, https://doi.org/10.1002/aenm.201400696.
- [23] J.Y. Cheong, W.T. Koo, C. Kim, J.W. Jung, I.D. Kim, Feasible defect engineering by employing metal organic framework templates into one-dimensional metal oxides for battery applications, ACS Appl. Mater. Interfaces 10 (2018) 20540–20549, https://doi.org/10.1021/acsami.8b04968.
- [24] J. Bae, D. Shin, H. Jeong, B.S. Kim, J.W. Han, H. Lee, Highly water-resistant Ladoped Co₃O₄ catalyst for Co oxidation, ACS Catal. 9 (2019) 10093–10100, https://doi.org/10.1021/acscatal.9b02920.
- [25] Q. Ke, D. Yi, Y. Jin, F. Lu, B. Zhou, F. Zhan, Y. Yang, D. Gao, P. Yan, C. Wan, P. Cui, D. Golberg, J. Yao, X. Wang, Manganese doping in cobalt oxide nanorods promotes catalytic dehydrogenation, ACS Sustain. Chem. Eng. 8 (2020) 5734–5741, https://doi.org/10.1021/acssuschemeng.0c00842.
- [26] Y. Luo, Y. Zheng, J. Zuo, X. Feng, X. Wang, T. Zhang, K. Zhang, L. Jiang, Insights into the high performance of Mn–Co oxides derived from metal-organic frameworks for total toluene oxidation, J. Hazard. Mater. 349 (2018) 119–127, https://doi.org/10.1016/j.jhazmat.2018.01.053.
- [27] S. Raha, M. Ahmaruzzaman, Enhanced performance of a novel superparamagnetic g-C₃N₄/NiO/ZnO/Fe₃O₄ nanohybrid photocatalyst for removal of esomeprazole: effects of reaction parameters, co-existing substances and water matrices, Chem. Eng. J. 395 (2020) 124969, https://doi.org/10.1016/j.cej.2020.124969.
- [28] Q. Deng, H. Li, K. Pei, L.W. Wong, X. Zheng, C.S. Tsang, H. Chen, W. Shen, T.H. Ly, J. Zhao, Q. Fu, Strategic design for high-efficiency oxygen evolution reaction (OER) catalysts by triggering lattice oxygen oxidation in cobalt spinel oxides, ACS Nano (2024), https://doi.org/10.1021/acsnano.4c14158.
- [29] S. Laruelle, S. Grugeon, P. Poizot, M. Dollé, L. Dupont, J.-M. Tarascon, On the origin of the extra electrochemical capacity displayed by MO/Li cells at low potential, J. Electrochem. Soc. 149 (2002) A627, https://doi.org/10.1149/11467947
- [30] H. Wang, N. Mi, S. Sun, W. Zhang, S. Yao, Oxygen vacancies enhancing capacitance of MgCo₂O4 for high performance asymmetric supercapacitors, J. Alloys Compd. 869 (2021) 159294, https://doi.org/10.1016/j.jallcom.2021.159294.
- [31] B. Liu, S. Sun, R. Jia, H. Zhang, X. Zhu, C. Zhang, J. Xu, T. Zhai, H. Xia, Oxygen-deficient homo-interface toward exciting boost of pseudocapacitance, Adv. Funct. Mater. 30 (2020) 1–9, https://doi.org/10.1002/adfm.201909546.
- [32] A. Navrotsky, C. Ma, K. Lilova, N. Birkner, Nanophase transition metal oxides show large thermodynamically driven shifts in oxidation-reduction equilibria, Science 330 (2010) 199–201, https://doi.org/10.1126/science.1195875.
- [33] J. Liu, H. Xia, L. Lu, D. Xue, Anisotropic Co₃O₄ porous nanocapsules toward high-capacity Li-ion batteries, J. Mater. Chem. 20 (2010) 1506–1510, https://doi.org/10.1039/b923834d.

- [34] A.N. Naveen, S. Selladurai, Investigation on physiochemical properties of Mn substituted spinel cobalt oxide for supercapacitor applications, Electrochim. Acta 125 (2014) 404–414. https://doi.org/10.1016/j.electacta.2014.01.161.
- 125 (2014) 404-414, https://doi.org/10.1016/j.electacta.2014.01.161.
 [35] I.C. Man, H.Y. Su, F. Calle-Vallejo, H.A. Hansen, J.I. Martínez, N.G. Inoglu, J. Kitchin, T.F. Jaramillo, J.K. Nørskov, J. Rossmeisl, Universality in oxygen evolution electrocatalysis on oxide surfaces, ChemCatChem 3 (2011) 1159-1165, https://doi.org/10.1002/cctc.201000397.
- [36] J. Hao, W. Wu, Q. Wang, D. Yan, G. Liu, S. Peng, Effect of grain size on electrochemical performance and kinetics of Co₃O₄ electrode materials, J. Mater. Chem. A 8 (2020) 7192–7196, https://doi.org/10.1039/d0ta02032j.
 [37] J.W. Jung, C.L. Lee, S. Yu, I.D. Kim, Electrospun nanofibers as a platform for
- [37] J.W. Jung, C.L. Lee, S. Yu, I.D. Kim, Electrospun nanofibers as a platform for advanced secondary batteries: a comprehensive review, J. Mater. Chem. A 4 (2016) 703–750, https://doi.org/10.1039/c5ta06844d.